ADVANCED FUNCTIONAL MATERIALS
www.afm-journal.de

# From Low Symmetry to High Dissymmetry: Chiral Plasmonic Films of Binary and Nanobipyramid Assemblies

*Martyna Wasiluk, Claire Goldmann, Maciej Bagiński, Mateusz Pawlak, PawełW. Majewski, Julia Abramowicz, Piotr Roszkowski, Lukas Rebholz, Carsten Rockstuhl, Cyrille Hamon,* and Wiktor Lewandowski**

**Thin films exhibiting plasmonic circular dichroism (PCD) represent a promising class of materials for technologies based on light processing. However, their potential is limited by the relatively low selectivity of interactions with circularly polarized photons of a given handedness and restricted tunability of the chiroptical properties. This article aims to resolve these problems with two innovations. First, it assembles gold nanobipyramids (NBPs), a promising building block for plasmonics, and arrange them in helical assemblies using a liquid-crystalline (LC) template. By optimizing the organic coating of NBPs, their size, and loading in the thin film, it achieves PCD films with state-of-the-art dissymmetry, g-factor on the order of $10^{-2}$. This study unequivocally evidence the properties by Mueller Matrix polarimetry and identify plasmonic coupling between particles as the driving force for the origin of the PCD properties using T-matrix theoretical modeling. Second, spectral and dynamic PCD engineering is achieved by varying particle sizes, co-assembling NBPs with nanospheres, and reversible melting and crystallization of the thin film. Overall, this work unlocks the potential of NBPs and binary assemblies based on NBPs for chiral plasmonics, providing a strategy for thin film materials displaying spectral and temporal PCD response with high dissymmetry factors.**

## 1. Introduction

Plasmonic circular dichroism (PCD) is emerging as a powerful tool for enhancing chiroptical effects at the nanoscale. PCD materials allow selective, dissymmetric interactions with circularly polarized light,[1] forming the foundation of future optoelectronic technologies.[2,3] This opens up significant potential in chiral sensing, enantioselective catalysis, and optical information processing. Several methods have been developed to fabricate PCD structures, usually relying on either the intrinsic chiral morphology of nanoparticles (NPs) and/or by assembling achiral NPs into chiral configurations.[4–19] Despite recent, rapid progress in this field, two significant challenges persist for practical applications.

The first challenge is developing materials with high dissymmetry factors, that is, materials that can effectively discriminate between the two circular polarizations of light. Achieving the normalized difference of the absorbance for left- and right-circularly polarized light (g-factors) on the order of $\approx 10^{-2}$ is not trivial.[20,21] However, it is a prerequisite to practical applications. The second challenge is gaining precise control of the spectral and dynamic aspects of the PCD response, which is essential for developing tunable and responsive chiral nanodevices. For example, highly dissymmetric PCD systems have recently been introduced.[20] Several systems, including cellulose nanocrystal thin films embedded with plasmonic nanoparticles,[22,23] stiff helical templates loaded with gold NPs,[5,24] layered assemblies of nanowires,[25,26] and intrinsically chiral plasmonic nanoparticles,[27,28] have demonstrated high dissymmetry factors, with |g| values reaching up to $10^{-1}$. However, these materials are functional only at the micro-scale and/or lack

M. Wasiluk, M. Bagiński, M. Pawlak, P. Majewski, J. Abramowicz, P. Roszkowski, W. Lewandowski
Department of Chemistry
University of Warsaw
Warsaw 02089, Poland
E-mail: wlewandowski@chem.uw.edu.pl

The ORCID identification number(s) for the author(s) of this article can be found under https://doi.org/10.1002/adfm.202500933



**DOI: 10.1002/adfm.202500933**

C. Goldmann, C. Hamon
Laboratoire de Physique des Solides
Université Paris-Saclay
Orsay 91405, France
E-mail: cyrille.hamon@universite-paris-saclay.fr

L. Rebholz, C. Rockstuhl
Institute of Theoretical Solid State Physics
Karlsruhe Institute of Technology
Kaiserstr. 12, 76131 Karlsruhe, Germany

C. Rockstuhl
Institute of Nanotechnology
Karlsruhe Institute of Technology
Kaiserstr. 12, 76131 Karlsruhe, Germany

dynamic tunability. Below, we outline potential strategies to address these challenges and guide the design of reconfigurable materials with high dissymmetry factors.

A particularly attractive method to enhance dissymmetry and tunability is varying the design of metallic components of PCD materials. Among different particle types, the unique shape and the resulting spectacular plasmonic properties of low-symmetry gold nanobipyramids (NBPs) make them particularly promising for PCD applications. Structurally, NBPs consist of two base-stacked pentagonal pyramids symmetrically, exposing sharp tips and exhibiting 5-fold rotational symmetry around the long axis[29] making them suitable for use in optical filtering,[30,31] ultrafast pulsed-lasers,[32] point-of-care bioassays,[33] plasmon-based sensing,[34–36] surface-enhanced Raman spectroscopy,[37,38] optoelectronics,[39,40] and fluorescence enhancement.[41] Moreover, the uniform shape and size of NBPs enable the fabrication of large-scale, ordered assemblies of Au NBPs, benefiting from directional[42–47] and/or collective[48] plasmon responses and aspect-ratio (AR) tunability. Recent studies have explored applying NBPs in PCD materials: by overgrowing NBPs into chiral morphology[16,49] or by the DNA-based assembly of NBPs.[50] These works confirm the beneficial properties of the low-symmetry and unique plasmonic responses of NBP in the context of PCD materials.

Unfortunately, NBPs are difficult to integrate into a particularly attractive form of PCD materials – macroscopic thin films. Such films are fabricated through a templated assembly, in which a chiral template guides the assembly of achiral particles. In this case, achieving dissymmetry enhancement and tunability is relatively straightforward, as both the template and nanoparticles contribute to the final properties. For example, varying the shape of nanoparticles from sphere to rod shifts the PCD band, even when using the same chiral template.[51] While introducing a dynamically switchable template component can lead to the dynamic shifting of PCD bands without changing the particle shape.[52] Why do NBPs resist assembling into PCD thin films? It is mainly related to their complex shape, which translates to the challenge of matching the NBP geometry and chemistry to that of the template. Further work concerning surface coating optimization, ensuring the colloidal stability of NBPs, and matching them with a proper template is required to enable the templated assembly of NBPs, and, thus, fully capitalize on the unique properties of NBPs.

Before analyzing the methods for assembling NBPs, one more aspect of the assembly-based approach for PCD materials is worth highlighting. All systems reported to date were prepared using one particle type at a time. In other words, these were unary-type assemblies, constrained by tying the PCD response to a single, most intense plasmonic absorption band. We hypothesize that achieving binary-type chiral systems assemblies may be a feasible way to modify PCD. Overall, achieving reconfigurable, strongly dissymmetric thin films and developing methods to go beyond single-absorption-related PCD response await discovery.

Among the different assembly approaches for forming chiral assemblies, liquid crystal (LC) matrices are gaining significant interest.[51,53] This method involves incorporating the NPs in the LC matrix and then drop-casting the material onto a given substrate. Upon heating to the isotropic melt and subsequent cooling, the LC molecules self-organize into a morphologically chiral supramolecular structure known as the helical nanofilament phase, which guides the NPs into a double-helical structure. This approach has two main advantages. First, it is relatively straightforward, rapid, cost-effective, reproducible, and adaptable to various NPs. Second, LC matrices enable dynamic reconfigurability, allowing for the creation of reversibly switchable structures with temperature- and light-responsive properties. With further advancements in the structural and chemical design of plasmonic components, the LC-based approach holds great potential for developing responsive, highly tunable, multicomponent and highly dissymmetric systems.[42,47]

In this work, we report efficient and reproducible methods for the chiral assembly of unary NBPs and binary plasmonic systems, resulting in highly dissymmetric and tunable PCD thin films. First, we performed the phase transfer (PT) of NBPs from the aqueous to organic solvent. We optimized the organic shell composition based on the stability of particles in the organic solvent and their compatibility with the LC helical template. The varied parameters included the dodecanethiol (DDT) to LC-ligand ratio and the overall amount of the ligands. The UV-Vis and TEM analysis confirmed that this process preserved the NBPs' morphology. Then, we demonstrated that NBPs with optimized coatings closely followed the LC template's morphology, forming plasmonic helical nanofilaments. We successfully created centimeter-scale homochiral films of helically arranged NBPs by adding chirality inductors to the mixture of LC and NBPs. Further, we showed that the strength of the PCD signals depends on the concentration, size, and shape of the NPs. Mueller Matrix (MM) polarimetry confirmed that the CD response originates from the helical arrangement of the NBPs. Based on a numerical model of the helical arrangements, we find that the chiral response is facilitated by plasmonic coupling between the nanoparticles. We further achieved binary chiral assemblies with broadened PCD responses by assembling two plasmonic components in a single film. Finally, we demonstrate the temporal control of PCD under thermal stimuli, showcasing the possibility of exploiting the unique properties of complex, polyhedral NPs in PCD composites. These results provide a promising route toward PCD systems for applications requiring strong dissymmetry, spectral tunability, and dynamic control.

## 2. Results and Discussion

### 2.1. Design and Fabrication of Chiral Nanocomposite Thin Films

The first step was the synthesis of the LC matrix for assembling NBPs. We have chosen to use the 4-[[(E)-[4-(octadecyloxy)phenyl]imino]methyl]-1,3-phenylene benzoate (OIM, **Figure 1b**). The synthetic route and detailed procedures are given in Figure S1 and Note S1 (Supporting Information). Upon cooling from the isotropic liquid, OIM first forms the B7 LC phase and then transitions to the helical nanofilament phase (Note S2, Supporting Information). This phase consists of supramolecular helical nanofilaments with a pitch of ≈230 nm, a width of ≈45 nm, and a thickness of ≈15 nm.

At the same time, we prepared a series of NBPs of various sizes. Since direct synthesis of hydrophobic, high-quality anisotropic NPs in an organic environment is challenging, an alternative is to obtain NPs in an aqueous environment first

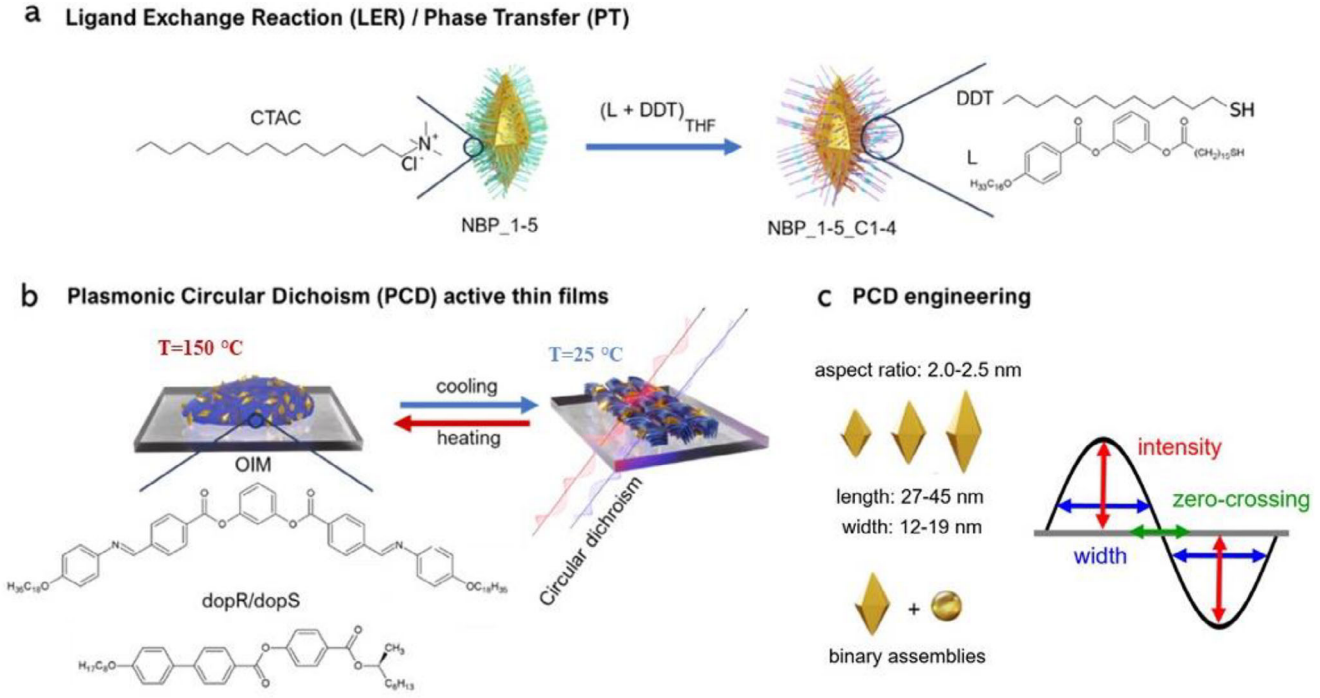


**Figure 1.** Scheme showing the engineering and formation of plasmonic circular dichroism thin films using nanobipyramids. a) Scheme of the Ligand Exchange Reaction (LER) / Phase Transfer (PT) required to ensure compatibility with the liquid-crystal matrix (from the left): cetyl trimethyl ammonium chloride (CTAC) coating nanobipyramids (NBPs) after the synthesis is exchanged to a binary mixture of alkyl (dodecanethiol, DDT) and liquid-crystal like (L) ligands resulting in phase transfer from a hydrophilic to a hydrophobic environment; molecular structures of CTAC, L, and DDT are shown. b) Scheme of Oleyl-Imine-Matrix, OIM doped with NBPs: (from the left) drop-casting and heating results in the dispersion of NBPs in the volume of melted OIM matrix, and subsequent cooling induces the formation of the helical nanofilament phase of OIM, in which the NPs fits; molecular structures of OIM and dopR/dopS (compounds used as chirality inducers) are shown. c) Engineering wavelengths and intensity of plasmonic circular dichroism (PCD) properties by varying the aspect ratio (AR)/size of the NBPs and by fabricating binary, chiral assemblies of NPs.

and then perform a simultaneous ligand exchange reaction with phase transfer (LER/PT). Thus, we synthesized a series of NBPs, utilizing the method described by Chateau et al.[54] We aimed at NBP sizes in the range of ≈27–48 nm length and ≈12–19 nm width. It should be noted that these particles were much larger than NPs previously arranged by helical LC matrices,[51,53] which required particular precision in achieving chemical compatibility with the matrix. As the protocol for forming helical nanostructures requires heat annealing, the NBPs were coated with a thin Ag layer, which has been shown to improve stability against thermal reshaping.[55] We initially obtained three batches of NBPs (NBP_1-3) of different sizes coated with the polar ligand cetyltrimethylammonium chloride (CTAC). A detailed analysis of the morphology and optical properties of the obtained NBPs is shown in the Supplementary Information (Figures S4 and S5, Supporting Information).

NBPs were then phase-transferred through the LER/PT process (schematically shown in Figure 1a). For coating NBPs we used a new LC-like ligand, 3-[(16-sulfanylhexadecanoyl)oxy]phenyl 4-hexadecyloxybenzoate (L, Figure 1a). The synthetic route and procedures are given in Figure S2 and Note S1 (Supporting Information). This ligand is a simplified version of the previously reported compound[53] (L2, synthetic route, and detailed procedures are given in Figure S3 and Note S1, Supporting Information), which was previously shown to facilitate the formation of helical assemblies of NPs driven by OIM.[51,53,56,57] L requires fewer synthetic steps and can be prepared with a higher overall synthetic yield.

We optimized the composition of ligand solutions for the LER/PT procedure to preserve the shape and size of NBPs while improving chemical compatibility with the LC matrix (detailed procedure and purification process are described in Note S3, Supporting Information). This process was particularly challenging given the highly anisotropic shape and relatively large size of NBPs. We tested four types of LERs: i) full coverage with the L (referred to as C1 coating), and ii) mixtures of L with shorter alkyl ligand-dodecanethiol (DDT, Figure 1a). In the latter case, we varied the molar ratio of L:DDT. We also varied the amount of ligand introduced to the reaction mixtures. Ultimately, we performed 3 LER/PT yielding binary organic coating layers. In these cases, reaction mixture formulation can be expressed as a molar ratio of Au atoms to L and DDT molecules ($Au^0$:L:DDT). We used 1:1:1, 1:2:2 and 1:2:1 ratios, for C2, C3, and C4 coatings, respectively.

At this point, it is worth rationalizing the choice of these particular binary mixtures of ligands for coating NBPs. First, LC-like ligands possess aromatic and alkyl parts, which we expect to ensure efficient interactions with nonpolar organic solvents and LC templates. Second, the shorter DDT ligands lower the grafting density of LC-like ligands, increasing their conformational freedom and interdigitation with the surrounding media; thus, DDT ligands enhance the shell's interactions with solvents and improve the alignment of LC-like ligands with the curved surface

of the helical nanofilament template. More detailed discussion about the importance of binary shell composition for forming the helical assemblies is given in Notes S3 and S4 (Supporting Information) and exemplified by additional experiments shown in Figure S10 (Supporting Information).

Before phase transfer, NBPs were highly monodisperse (max size distribution ≈6%) with slight tip truncation, which increased for smaller NBPs as expected (Figure S5, Supporting Information). After phase transfer, NBPs retain their shape with only a slight rounding of the NBP tips, minor changes of dimensions (≈6–9%), and variable aspect ratios (up to ≈20% for the smallest NBP_1 and below 10% for larger NBP_2 and NBP_3; see Figures S5–S8 and Table S1, Supporting Information for more details).

After LER/PT, we also analyzed in detail the colloidal stability of all obtained materials by performing a series of UV–vis measurements over 7 days (Figure S9 and Table S2, Supporting Information). While plasmonic properties were retained for C2-C4 in the case of L-based coatings, weaker colloidal stability was observed in all hybrids based on L2 ligand and C1 coating.

### 2.2. Optimizing the Composition to Enhance the Chiral Plasmonic Properties

Further choosing of the optimal particle coating of the phase transferred NBPs with the LC template was then assessed by following the particle distribution within the composite. When NBPs exhibit good chemical compatibility, they disperse uniformly in the heated LC film and align along the growing helical nanofilaments during cooling (Figure 1b). This behavior was not observed for the NBP_2_C1 particles (**Figure 2**a), which phase-separated from the LC matrix, indicating poor chemical compatibility. In contrast, samples NBP_2_C2-C4 showed significantly improved distribution within the OIM matrix, featuring a combination of randomly oriented and linear assemblies (Figure 2b,c; Figures S11,S12, and S17, Supporting Information). In the case of NBP_2_C4, linear assemblies were predominantly observed.

To more quantitatively evaluate the chemical compatibility of chosen materials with the LC matrix, we compared the chiroptical properties of thin film composites prepared using NBP_2 with different coatings. Thus, NBP_2_C1-4 were mixed with a solution of helical template – OIM and chiral dopant directing the handedness of the helical nanofilaments formed by OIM (the samples comprised 18 wt.% NBPs and 10 wt.% of a dopant). We used chiral dopants: either (S) or (R)-(4)[(Methylheptyloxy)carbonyl]phenyl-4′-octyloxy-4-biphenylcarbohylate (Figure 1b) – called dopS and dopR, respectively. Importantly, the presence of the chiral dopant is required to form macroscopic chiral films since, without the dopant, a racemic mixture comprising microscopic domains of the opposite handedness is formed. The macroscopic CD signal is negligible in the racemic case, as expected for the conglomerate structure. Whereas, if the dopant is used, it interacts with the template molecules at each nucleation point. Depending on the handedness of the dopant, it exerts a torque, which leads to the favoring of right- or left-handed twist of the crystallite. Then, the avalanche-like growth of the helical nanofilaments amplifies the twist from the nucleation point, through a dendritic growth.[51,58,59] The filament twist is then transferred to NBPs, which should follow the helical contour of the filaments.

Indeed, each of the obtained samples based on NBP_2_C1-4 NPs exhibited extinction characteristic to the absorption of NBPs (Figure 2g) and corresponding Cotton-shaped CD signals in the plasmonic range[60] (Figure 2i) with $\sigma-/\sigma+$ characteristics, with a minimum at ≈658 nm and maximum at ≈743 nm. Zero crossing was found at ≈695 nm, in the range of the maxima of the longitudinal modes of NBPs. While the spectral positions of the PCD bands were similar for all studied cases, the signal magnitude varied depending on the NPs surface coverage. The highest (absolute) CD values were recorded for NBP_2_C4 sample (Figure 2i). To more objectively compare the different samples, we calculated the extinction dissymmetry factor (g-factor, $g_{ext}$), defined as $g_{ext} = 2(EL - ER)/(EL + ER)$, where EL and ER are the extinctions measured for left and right polarized light, respectively. The maximal absolute values of the g-factor were calculated for all analyzed materials (inset in Figure 2i), indicating that the C4 coating is optimal for maximizing the dissymmetry of the thin film. Results of the further experiments of the optimization process, such as loading of the chiral dopant and heat-annealing rate, are shown in the Figures S14–S16 (Supporting Information).

As the next parameter, we decided to verify how particle loading can influence the strength of the PCD signal. A series of thin films with varying NBP_2_C4 concentrations, from 2 wt.% to 25 wt.% was prepared. These films exhibited characteristic extinction bands of NBPs and corresponding Cotton-shaped CD signals in the ranges characteristic of organic template and nanoparticles (Figure 2h,j; Figure S17 and Note S5, Supporting Information). Analysis of the chiral plasmonic properties revealed that CD and g-factor values increased with NPs loading up to 18 wt.%, after which they declined. This can be explained when arguing that coupling between the NBPs is responsible for the observed chiroptical properties, which we confirm and further explore in Section 2.4. Shortly, the increase of particle content up to 18 wt.% translates to an increased chiroptical response driven by the overall rise in plasmonic coupling bewteen particles. Above this threshold, the amount of particles not aligning along the filaments, but forming clusters, increases. In such a case, the clustering may introduce large deviations from the helical arrangements or, generally, geometrically chiral arrangements, leading to the deterioration of the chiral optical signal. In line with this interpretation, TEM images show a growing tendency to form clusters for the increasing particle content (Figure 2d–f; Figure S17, Supporting Information).

After optimizing the nanocomposite materials, we explored the possibility of maximizing the PCD signal intensity and spectral tunability. First, we investigated the effect of using NBPs with different sizes. For this purpose we prepared samples consisting of a predetermined amount of LC matrix, chiral dopants (10 wt.%, either dopS or dopR), and an optimal amount (18 wt.%) of NBPs with C4 shell in three sizes NBP_1, NBP_2, and NBP_3 (in ascending order of size). TEM analysis of each sample showed that NBPs were well-dispersed within the organic matrix, forming predominantly linear assemblies, irrespective of their size (**Figure 3**a–c). This indicates that the helical nanofilaments effectively guided the spatial organization of the NBPs, proving the efficiency of the optimized surface coating and composite annealing procedure. The successful dispersion of the particles

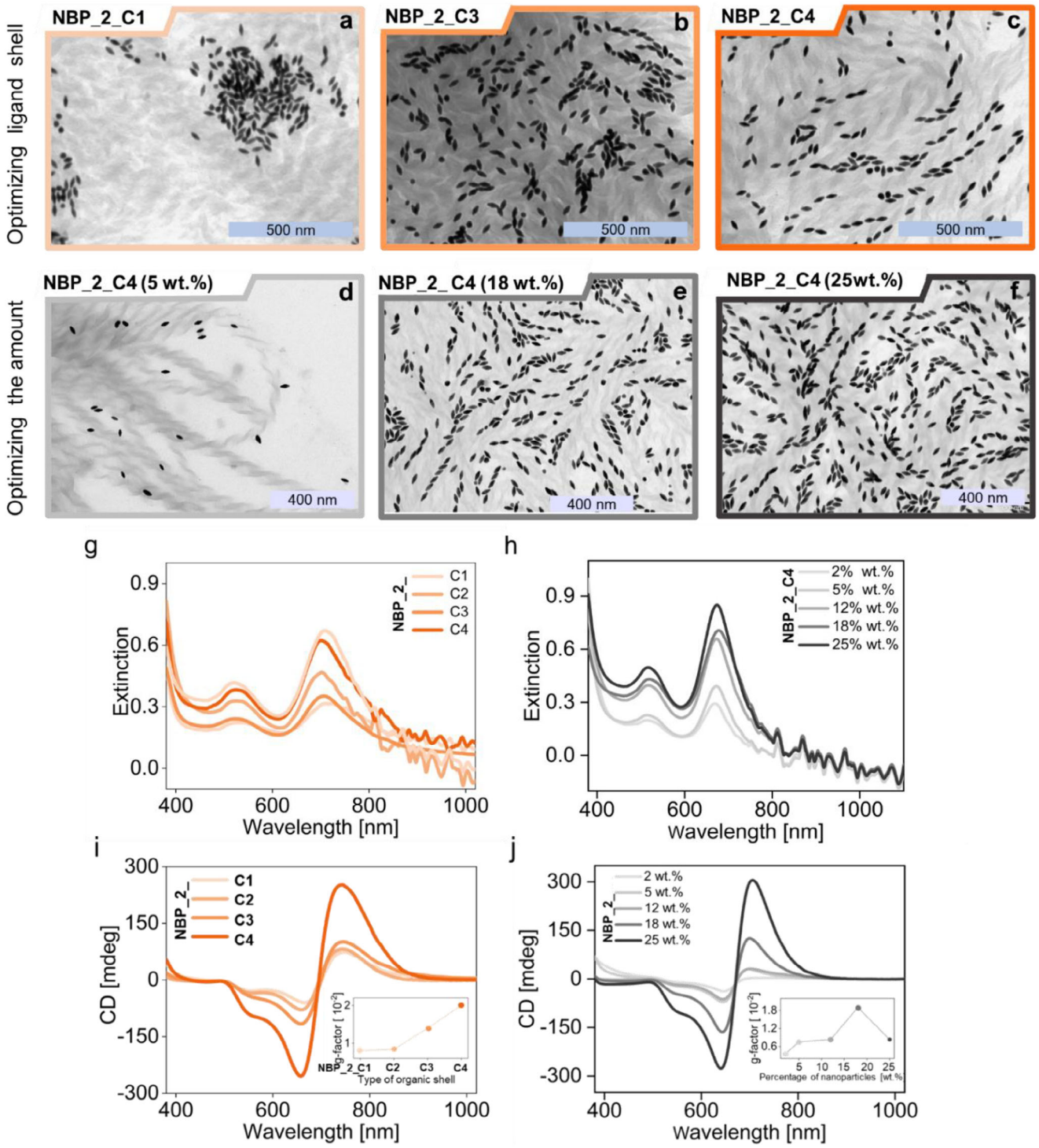


**Figure 2.** Optimizing the organic shell of NBPs and their content in chiral nanocomposites. a-c) TEM micrographs of OIM helical fibers decorated with NBP_2 covered with various types of L:DDT mixtures: (a) NBP_2_C1, (b) NBP_2_C3, and (c) NBP_2_C4. d-f) TEM micrographs of composites containing: (d) 5, (e) 18 and (f) 25 wt.% NBP_2_C4 and 10 wt.% chiral dopant S. g,i) Extinction and circular dichroism spectra of composites prepared with NBPs having different ligand coatings and chiral dopant S; the maximal g-factor values corresponding to these results are provided in the inset. h,j) Extinction and circular dichroism spectra for materials comprising 2, 5, 12, 18, 25 wt.% NBP_2_C4 and 10 wt.% chiral dopant S; the maximal g-factor values corresponding to these results are provided in the inset.

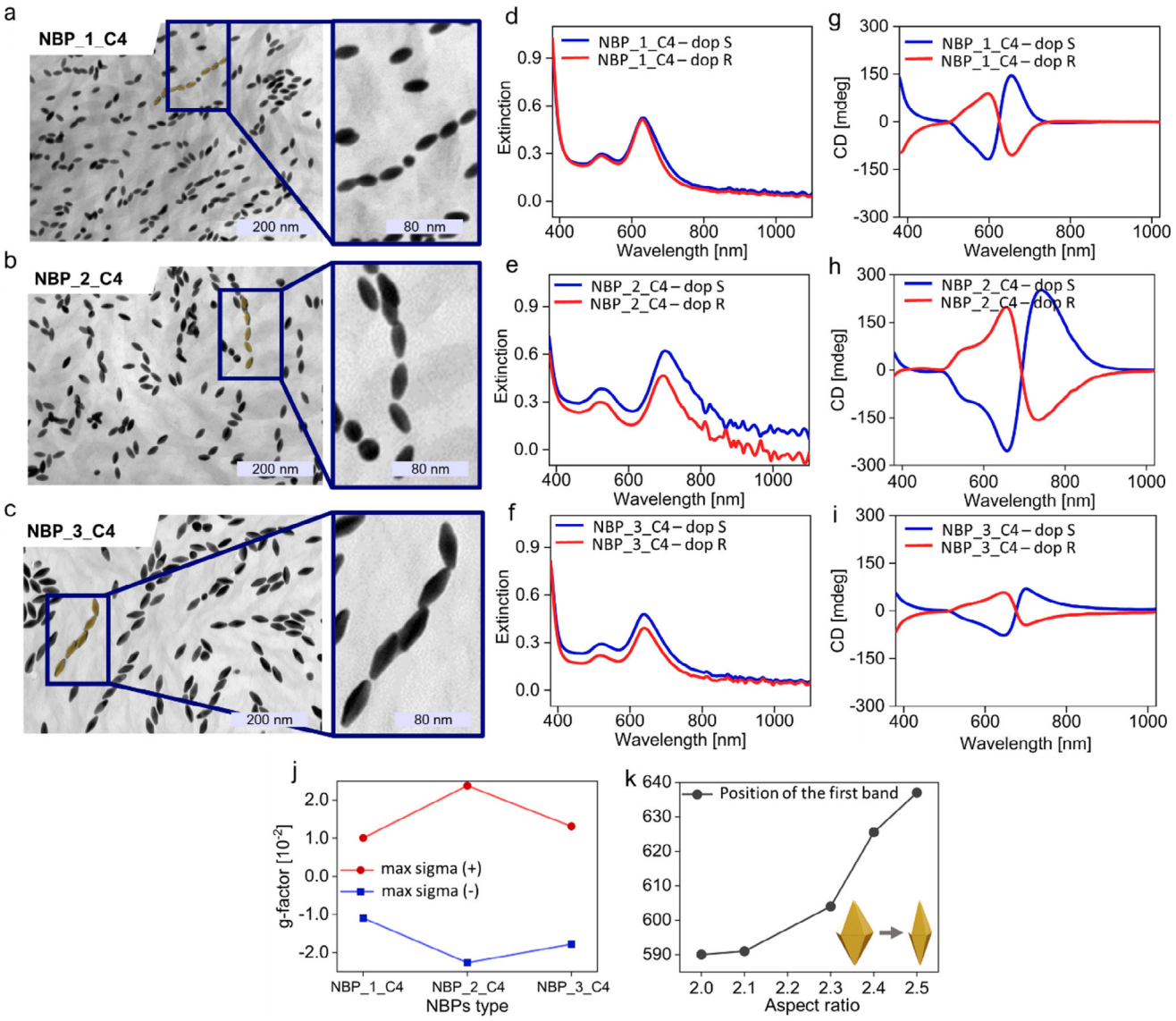


**Figure 3.** Engineering PCD response by varying the size and aspect ratio of NBPs. TEM micrographs of OIM-based composites comprising 18 wt.% of a) NBP_1_C4, b) NBP_2_C4, and c) NBP_3_C4. d-f) Extinction and g-i) CD spectra of chiral OIM-based nanocomposites with either 10 wt.% of dopR (red lines) or dopS (blue lines) and 18 wt.% of (d,g) NBP_1_C4, (e,h) NBP_2_C4, and (f, i) NBP_3_C4. j) Graph showing the dependence of maximal g-factor value for $\sigma-$ and $\sigma+$ bands of CD spectra shown in panels g-i; lines are for eye guidance only. k) Graph showing the spectral dependence of the plasmonic band maxima on the aspect ratio (AR) of the NBPs; lines are for eye guidance only. Additional data are provide in Figure S18, Supporting Information.

in the volume of the material was further supported by UV-Vis measurements, which revealed plasmonic bands characteristic of NBPs (Figure 3d–f). PCD measurements revealed strong chiroptical response across all samples (Figure 3g–i). The g-factor value for samples NBP_1, NBP_2 and NBP_3 were $1.1 \times 10^{-2}$, $2.3 \times 10^{-2}$ and $1.7 \times 10^{-2}$, respectively (Figure 3j). Note that multiple aspects can influence the strength of the chiroptical response, such as extinction cross-sections, compatibility with the matrix, or the level of deviations from the ideal helical geometry of the assemblies (which cannot be quantified with high confidence). Thus, we limit our conclusions to noting that NBP_2 particles provided the highest dissymmetry among the tested systems.

In the context of spectral control of the PCD phenomena, it is important to emphasize that the NBPs used in this study exhibit varying ARs, allowing for tunability of the PCD response. To explore this, we included two additional batches of NBPs (NBPs_4 and NBPs_5), enabling the preparation of samples with ARs ranging from 2.0 to 2.5 (structural and optical data for these samples are presented in Figures S8 and S19, Supporting Information). As expected, the plasmonic bands of the NBPs are dependent on the AR. Crucially, this translates to the spectral modulation of the PCD response. Specifically, the zero crossing and maxima of the CD bands shifted by ≈40 nm (Figure 3k) with varying AR, underscoring the composites' spectral tunability.

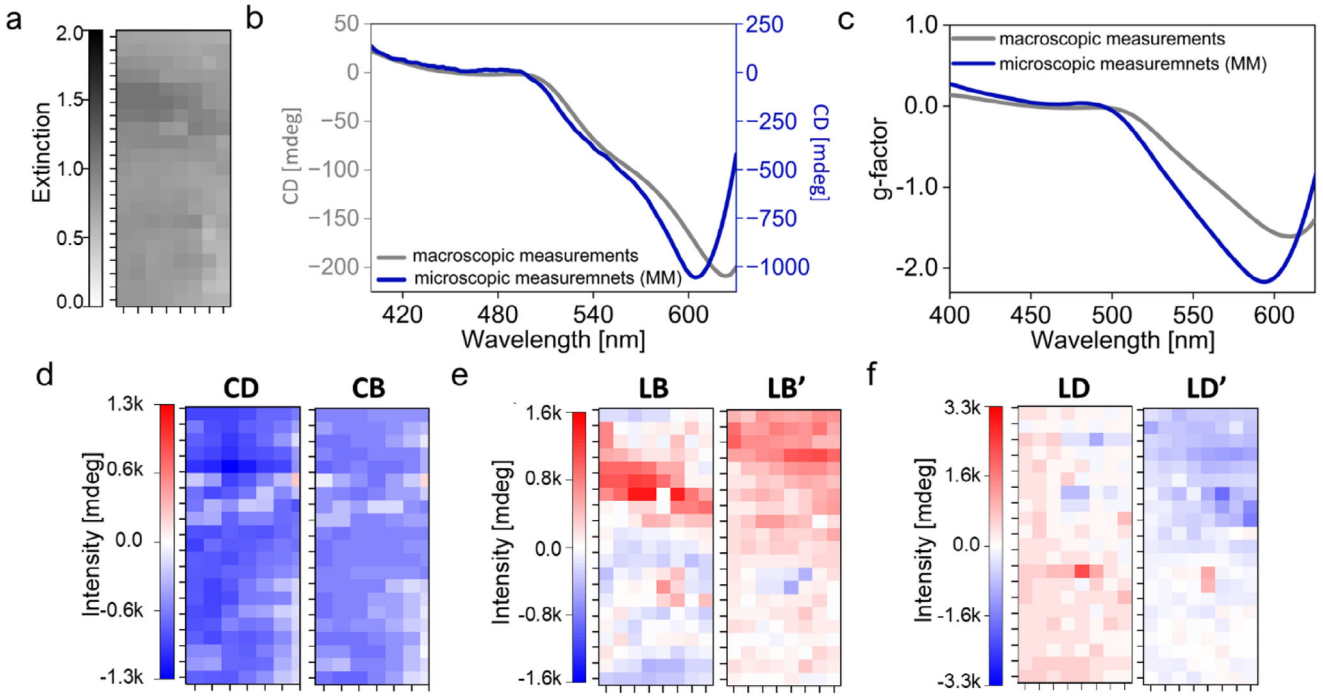


**Figure 4.** Detailed optical investigation of PCD films using Mueller Matrix (MM) polarimetry. a) A map of the extinction measured at 630 nm, collected for the area of 325 × 1050 μm$^2$. b) CD spectra for the same sample collected with an in-house CD spectrometer (macroscopic measurements) and derived from the MM polarimetry (microscopic measurements); c) G-factor graphs for CD shown in panel b. d) CD and CB, e) LB and LB and f) LD and LD' maps measured with MM polarimetry for the area shown in panel a.

To finalize this part, we wish to highlight the impact of NBP geometry on the PCD dissymmetry, with respect to other types of NPs. As a "control" experiment, we prepared a composite film using gold nanorods. These particles had a similar volume to NBP_2, they were covered with the same ligand shell, and we optimized their loading in the composite; all in order to arrive at the maximal possible dissymmetries. Based on the electron microscopy images we conclude that these thin film composites exhibited structural characteristics similar to NBPs. However, the maximal recorded g-factor values were almost an order of magnitude lower than those observed for NBPs (Figure S20, Supporting Information). Thus, we can conclude that the shape and resulting plasmonic properties of NBPs are crucial features enabling the strong PCD response in composites.

### 2.3. Disentangling Optical Properties by Mueller Matrix Polarimetry

Measurements of the chiroptical properties of thin-film materials are known to be prone to artifacts arising from circular birefringence (CB), linear birefringence (LB), and linear dichroism (LD). To mitigate these issues, it is standard practice to perform circular dichroism (CD) measurements multiple times for a single sample, rotating the sample within its plane and flipping it (Figure S21, Supporting Information). This approach allows for a preliminary exclusion of strong contributions other than CD, though it assumes that all these parameters are independent. To fully resolve this issue, a state-of-the-art method called Mueller Matrix polarimetry can be employed, in which the optical properties of samples are calculated from Mueller matrices using a differential method.[61] The differential MM of non-depolarizing material is G-antisymmetric and decomposes the optical properties into elementary contributions, including circular dichroism, circular birefringence (CB, **Figure** 4d), and pairs of linear birefringence (LB, LB', Figure 4e) and linear dichroism (LD, LD', Figure 4f) values. LB' and LD' values are measured in a coordinate system rotated by 45 degrees relative to the initial orientation. We performed these measurements on a selected thin-film composite over 50 × 50 μm$^2$ area, covering the spectral range of 400–630 nm. The CD calculated from MM polarimetry for the NBPs assembled in the LC matrix showed two bands: a positive band in the range of ≈350–400 nm, originating from the chiral organic matrix, and a negative band between ≈500 and 650 nm, which can be attributed to the chiral assembly of gold NBPs (Figure 4b). Notably, the characteristic shape of the PCD response in CD (Figure 4b), as well as the shape and calculated values of PCD g-factors (Figure 4c), were in very good agreement with the results obtained for the macroscopic sample using our in-house CD spectrophotometer. Unfortunately, we could not collect MM at longer wavelengths due to the limitations of the MM polarimetry set-up at the synchrotron facility. However, the very good agreement of the sigma-band suggests that all the above-presented data using the simplified approach of sample rotation and flipping are fully valid for the entire spectral range of PCD response.

Additionally, we leveraged the high resolution of the MM method to examine the uniformity of optical properties of the

film. For this purpose, we measured Mueller matrices at a wavelength of 630 nm with a spatial resolution of 50 µm. The absorbance map calculated from the diagonal elements of MM polarimetry (Figure 4a) revealed sample heterogeneities, which may result either from the imperfect thickness of the sample or the imperfect dispersion of NPs in the organic matrix. The spatial distribution of CB coincides with that of CD, suggesting that the helically assembled NBPs also contribute to the CB of the sample.

Further, information about the anisotropy of the sample can be extracted in the form of LD, LD', LB, and LB maps. Although inhomogeneities are visible, they are localized at different points than those observed on the CD, CB, and absorbance maps. Therefore, the observed anisotropy likely results from bundles of parallel helices within the sample. Since the sample is not oriented globally, many birefringent/dichroic domains resulted in the significant spatial distribution of LD, LD', LB, and LB'. Nevertheless, after averaging in macroscopic measurement they do not introduce significant apparent component into the recorded CD spectra.

### 2.4. Modeling of Chiral Plasmonic Properties

To gain a fundamental understanding of the chiral plasmonic properties of nanoparticle assemblies, we study the optical properties of the fabricated helical arrangements by simulations. For that purpose, we use a T-matrix-based multiple scattering framework. Here, we first study the optical response of the individual nanoparticles and compute their T-matrices. In our treatment, we approximate the gold NBPs as prolate ellipsoids with the same size and axis ratio. Such description reduces the computational effort by exploiting the axial symmetry and mitigates issues associated with sharp edges—features that are both numerically challenging and not prominently observed in the TEM images of composites. Such a description does not change the conclusions to be drawn, as the nanoparticles anyhow are entirely characterized by an electric dipole moment in their response.

The ellipsoids were dimensioned to emulate NBPs with an aspect ratio of 2.5, with a long axis radius of 16.5 nm and short axis radius of 6.5 nm. The optical properties of Au, interpolated from the data provided at https://refractiveindex.info,[62] were assigned to the nanoparticles. The particles were embedded in a homogeneous non-dispersive medium of refractive index $n = 1.6$ to simulate the surrounding organic thin film. The T-matrix of the individual nanoparticles are computed using the commercially available software JCMsuite that solves Maxwell's equations using the finite-element method.[63] Once the T-matrix is known, all the optical properties of the isolated nanoparticles can be extracted.[64] The T-matrices are stored in a community-agreed data format[65] and uploaded to a publicly available data repository at https://tmatrix.scc.kit.edu.

Optical simulations of individual nanoparticles, obtained via orientational averaging of the extinction cross section as shown in **Figure** 5a, exhibit two resonant features: a transverse resonance near 520 nm arising from electric dipolar oscillations along the short axes (x and y, which are two-fold degenerate), and a longitudinal resonance near 700 nm corresponding to the dipolar mode along the long axis (z). These features reproduce the features of resonances recorded for dispersions of NBPs qualitatively well. The ellipsoids serve as the basis for further investigation into how nanoparticle assemblies behave when arranged in chiral configurations.

As the chiral model, we have chosen to assemble seven nanoparticles spatially arranged along a helical path with their long axes oriented tangentially to the helix. The helix is defined by a pitch of 230 nm and a centerline radius of 29 nm—a distance chosen to mimic the idealized arrangement of nanoparticles if they were located along the edges of the organic helical nanofilaments. A detailed illustration is shown in Figure 5b. We considered several such assemblies with varied spacing of the ellipsoids. In the most condensed state, the winding number was 0.79, which yielded a center-to-center spacing of ≈38.22 nm between adjacent nanoparticles and a tip-to-tip air gap of roughly 5 nm. Moreover, to investigate the influence of inter-particle spacing on the strength of the CD signal, we varied the winding number of the helical path while keeping other parameters constant. In other words, increasing the winding number increased the center-to-center distances between nanoparticles, up to 91.66 nm, which corresponds to a tip-to-tip gap of roughly 75 nm. All the simulations of the chiral ensembles of nanoparticles are made using the publicly available software treams.[66]

To probe the chiral plasmonic response, circularly polarized plane wave illumination was simulated for both left-handed (LH) and right-handed (RH) polarization states, with the incident wave vector oriented perpendicular to the helix axis, parallel to the x-axis. For each polarization state, extinction cross-sections were computed. The resulting spectral analysis (Figure 5c, showing the handedness-averaged extinction cross section) revealed that the extinction peak corresponding to the longitudinal mode was shifted relative to an isolated nanoparticle. The shift decreases with an increasing spacing between the particles. However, we should note that even though the computed spectra for the most distant spacing considered appear very similar to the one of an isolated ellipsoid, coupling between particles is still observed.

Finally, we evaluated the circular dichroism defined as the difference between the left-handed and right-handed extinction cross section, CD = LH − RH, and the dissymmetry (g-) factor given by g = 2(LH − RH)/(LH + RH), as shown in Figure 5d,e. We identified a characteristic bisignate pattern (or Cotton effect) in the 700–800 nm spectral range. The analysis of the average extinction cross-section demonstrated a gradual deformation and shift of the resonant feature associated with the longitudinal mode. Concurrently, the g-factor exhibited notable changes in magnitude and spectral position, with the bisignate CD pattern shifting as a function of inter-particle distance. The observable trend in the extremal values of the g-factor underscored the sensitivity of chiral plasmonic responses to nanoparticle spacing.

In conclusion, our theoretical modeling reveals that the optical response of chiral nanoparticle assemblies is governed by the interplay between individual nanoparticle resonances and inter-particle coupling, strongly dependent on the spatial arrangement and inter-particle distances (Figure S22 and Note S6, Supporting Information). It specifically shows that the chiral optical response of the helical arrangements is facilitated by plasmonic coupling between the nanoparticles. Based on a T-matrix framework for

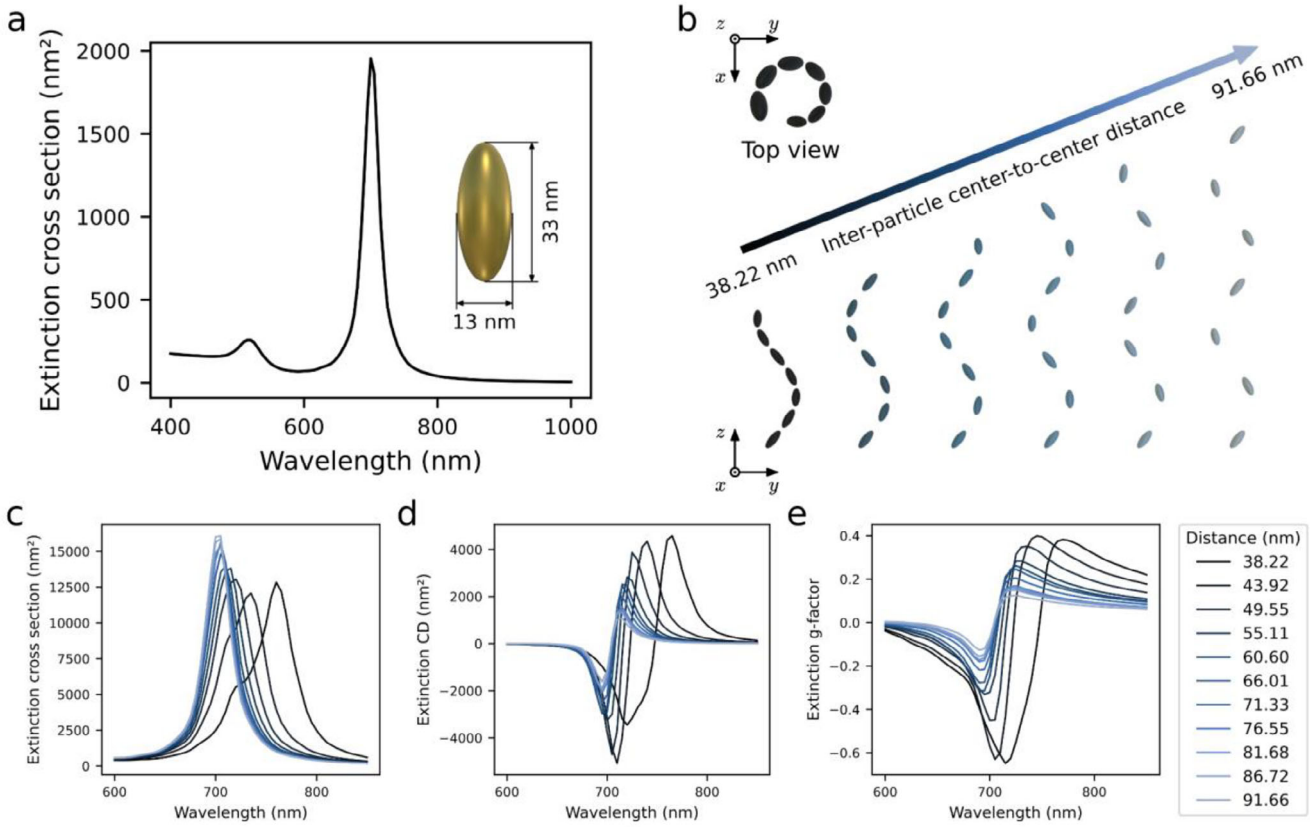


**Figure 5.** Numerical modeling of the chiral optical response of helically arranged plasmonic nanoparticles. a) Orientationally averaged extinction cross section of an isolated ellipsoidal gold nanoparticle. b) Depiction of helical arrangements of seven nanoparticles each, with increasing inter-particle distance. c) Extinction cross section, d) extinction circular dichroism, and e) extinction g-factor for radial illumination (wave vector parallel to x-axis) of helical arrangements for increasing inter-particle distance.

ellipsoidal nanoparticles, the simulations capture the essential features of the experimentally observed plasmonic circular dichroism, notably the spectral shifts and bisignate signatures in the longitudinal mode region. While this model provides valuable insight into the mechanisms at play, it also highlights the challenges in achieving perfect structural order experimentally; the g-factor values observed experimentally, which are an order of magnitude lower in comparison to theoretical predictions, are likely due to the imperfections in nanoparticle alignment and distribution within the helical assemblies.

### 2.5. Engineering Chiral Plasmonic Properties Using the Binary Assemblies Approach

The above-discussed results reveal several advantages of chiral composites based on NBPs. However, a limitation is that the PCD response is intrinsically linked to their main plasmonic band. Thus, to potentially achieve a chiral response tunability that extends beyond the capabilities of systems based on a single type of NPs, we explored the idea of fabricating binary, helical assemblies of nanoparticles. Compared to previously described binary assemblies relying on shape- or ligand-matching particles,[67–70] we aimed to form binary assemblies guided by the helical template. To this end, we considered systems consisting of NBPs and nanospheres (NSs). An excess mass percentage of spheres was used due to the significant disparity in the strengths of the PCD signals between these NPs and NBPs (NBPs produce signals an order of magnitude stronger than NSs). Thus, the mass percentage of NSs was kept constant at 23 wt.%, while the added amounts of NBPs were 1.25, 2.5, 5, and 7.5 wt.%. Analysis of TEM micrograph (**Figure 6a**) revealed that NSs readily align in linear formations and wrap around the surface of the helical nanofilaments. At the same time, NBPs coexist within these arrangements, joining the paths formed by NSs. When analyzing the PCD spectra (Figure 6b), we note that within the $\sigma+$ signal of the binary helical assemblies progressively changes with varying sample content. For the lowest concentration of NBPs, $\sigma+$ band overlays with what was expected for NSs (a relatively weak band centered at ≈630 nm). With increasing the NBP content, $\sigma+$ band blueshifts (to ≈680 nm) and increases intensity, more and more resembling the band coming from unary NBP sample. Conversely, the $\sigma-$ band seems to deviate from this tendency, closely resembling the band originating from the spheres alone. Overall, these results reveal that PCD spectral tunability can be achieved by adjusting the mass ratio of two types of nanoparticles, offering an additional level of tunability. These promising results motivated us to extend the experiment to another pair of particles, particularly nanorods and NSs. We describe this system in the Note S7 and Figure S20 (Supporting Information).

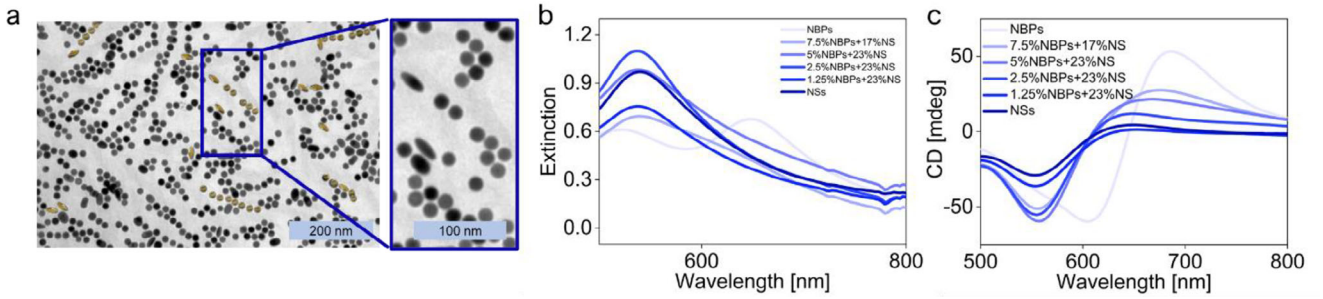


**Figure 6.** Engineering PCD through binary assemblies approach. a) TEM micrograph of OIM-based composites comprising nanospheres (23 wt.%) and NBP_2_C4 (5 wt.%). b) Extinction and c) CD spectra of chiral OIM-based nanocomposites with dopS (10 wt.%), comprising either nanospheres (NSs), NBP_2_C4 or binary mixtures of: NSs (23 wt.%) doped with varying amounts of NBP_2_C4 (1.25, 2.5, 5, 7.5 wt.%).

### 2.6. Engineering On–Off Chiral Plasmonic Properties Using Thermally Driven Structure Switching

Finally, we return to the unary systems to verify that they exhibit dynamic tunability in response to external stimuli. For this purpose, we performed 20 thermal annealing cycles on a selected, NBP_2_C4 sample. A scheme showing material behavior during reversible heating/cooling cycles, with 30 and 9 °C $min^{-1}$ heating and cooling rates, respectively, is given in **Figure** 7a. During each cycle, extinction and CD measurements were conducted at room temperature, where the matrix forms helical nanofilaments, and at 150 °C, where the matrix is in a molten state (Note S4, Supporting Information).

UV-vis measurements revealed that melting the sample causes a blueshift of the plasmonic band (Figure S23, Supporting Information), which suggests limiting the plasmonic coupling between NBPs and their efficient dispersion. This effect is reversed upon cooling the sample. The CD results (Figure 7c) evidenced that these extinction changes are driven, on–off switching of the PCD properties. Specifically, at low temperatures, the CD spectrum is characteristic of that reported above for the chiral systems, while at elevated temperatures, the CD readout is zero across the measured wavelengths.

We note that in successive cycles, the extinction and CD band maxima slightly shifted toward shorter wavelengths, while the calculated absolute values of the g-factor slightly decreased

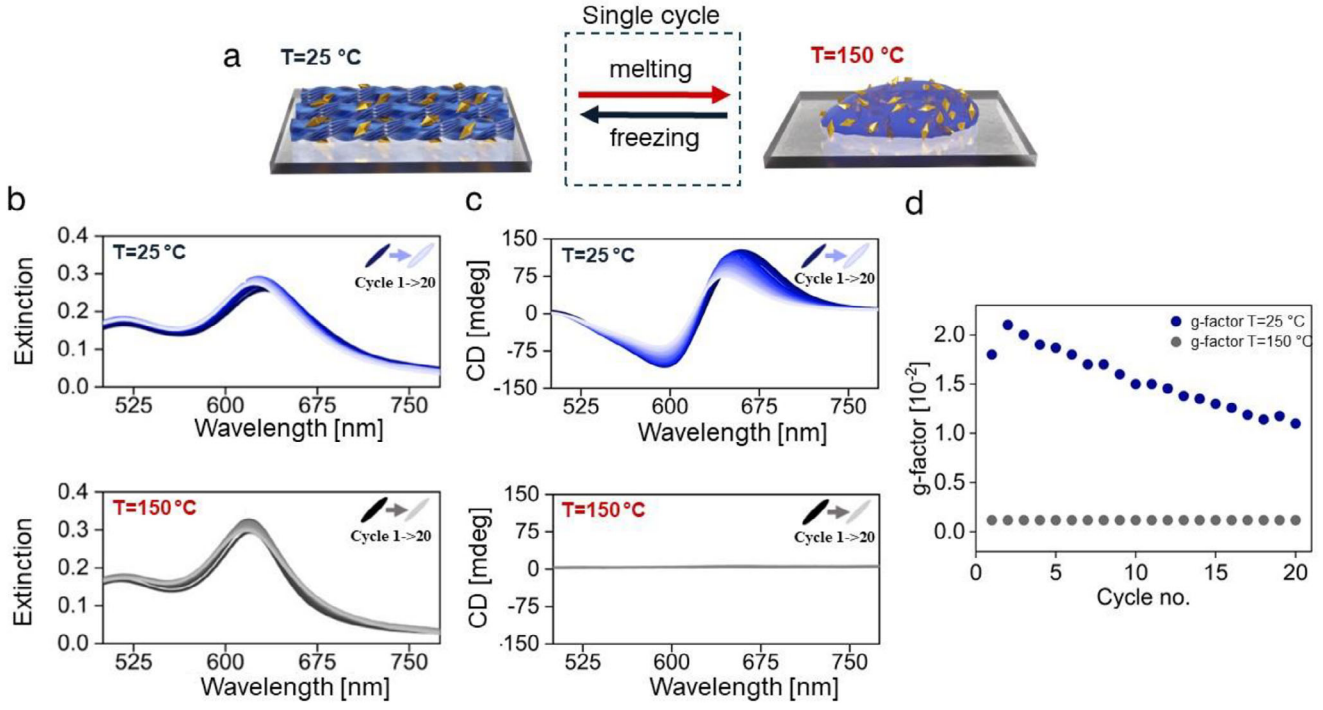


**Figure 7.** Reversible, on–off, thermally driven switching of the PCD response of chiral composites. a) A scheme of melting/freezing of the composite; the bracket around arrows represent a single cycle, which encompasses heating the sample to 150 °C and cooling down at a controlled rate to room temperature, ≈25 °C. b) Extinction and c) CD spectra obtained for the same sample over 20 thermal annealing cycles, at low (blue) and high (gray) temperatures. d) Graph showing the evolution of the maximum value of g-factor at low (blue) and elevated (gray) temperatures.

(Figure 7d). This phenomenon could be attributed to the shape-shifting of the NBPs or variations in particle assembly. Given the reproducibility of the plasmonic bands in consecutive cycles, as followed by UV-Vis spectra (Figure 7b), it seems plausible to conclude that the switching process does not affect the shape of the NBPs. Therefore, we attribute the variable CD/g-factor readout to an increasing tendency of the particles to form side-to-side arrangements, which is further supported by the longitudinal absorption band maxima slowly shifting toward shorter wavelengths in consecutive runs.

It should also be highlighted that these results demonstrate not only the possibility of switching PCD properties but also provide evidence of the genuinely remarkable thermal stability of the NBPs, considering that the sample was kept above 100 °C for 3 h to perform 20 switching cycles.

## 3. Conclusion

This work describes the efficient formation of chiral assemblies of nanobipyramids using a chiral liquid crystal matrix. First, the proposed phase transfer conditions and the organic shell composition of the NBPs provide both thermal reshaping resistance and colloidal stability. Furthermore, we demonstrate that modifications to the surface chemistry of NBPs significantly impact their assembly within the helical fibers formed by the LC matrix and the chiral optical response of the composites. We also studied the relationship between the size of the NBPs and the amplitude of the chiral response. This relationship is nonlinear because the chiroptical activity depends not only on the extinction cross-section of the NBPs but, more importantly, on the quality and uniformity of the formed helical nanostructures. Utilizing state-of-the-art chiroptical spectroscopy tools such as Mueller Matrix polarimetry, we have shown that the potential applications of plasmonic NBPs to achieve a highly dissymmetric plasmonic circular dichroism response with g-factor values on the order of $10^{-2}$. We have numerically modeled helical arrangements of plasmonic nanoparticles and show that the chiral optical response is facilitated by coupling between the nanoparticles.

Further, we demonstrated the possibility of spectral tuning the plasmonic circular dichroism response by changing the aspect ratio of NBPs, which shifts the maximum of the CD signal toward longer wavelengths as the aspect ratio increases. Intending to broaden the tunability further, we explored the formation of binary chiral assemblies. Finally, we confirm that these systems are highly durable and exhibit dynamic reconfigurability in the solid state, leading to a switchable PCD response. We also note that NBPs composite films displayed superior PCD dissymmetry enhancement in comparison to gold nanorods, showing that the intricate shape of NBPs provides an improved route to tune g-factors.

Overall, using the helical nanofilament template offers three key benefits: ultrathin, transmission-mode films, plasmon-driven chirality that can be tuned via nanoparticle morphology, and thermal reconfigurability, enabling thermal switching of the chiral response. Thus, the presented results pave the way for future developments of photonics based on plasmonic circular dichroism by uncovering the benefits of using switchable chiral matrices, the beneficial properties of NBPs, and their binary chiral assemblies.

## 4. Experimental Section

*Materials and Methods*: Silver nitrate ($AgNO_3$ ≥ 99%), tetrachloroauric acid ($HAuCl_4$ ≥ 99%), hydrochloric acid (HCl 36.5–38%), hexadecyltrimethylammonium bromide (CTAB, ≥ 99%), ascorbic acid (AA, ≥ 99%), benzyldimethylhexadecylammonium chloride (BDAC 99%), hexadecyltrimethylammonium chloride (CTAC, 25 wt.% in water), tetrahydrofuran (THF, anhydrous, ≥ 99.9%). All chemicals were used without further purification. Milli-Q water was used in all experiments.

*Bipyramid Synthesis and Purification*: AuBPs were synthesized by seed mediated growth as described previously.[43,48,71–73]

1) Seeds. In a bottle, 99 mL of water and 8 mL of CTAC 25 wt.% were mixed and put at 30 °C. 12 mL of $Na_3Cit$ 50 mM, followed by 1200 µL of $HAuCl_4$ 25 mM were added and after 30 min, under vigorous stirring, 1 mL of $NaBH_4$ 25 mM was added very quickly. After 2 min of stirring, the bottle was closed and the reaction medium was kept at 40 °C for 5 days.
2) Growth. In an Erlenmeyer flask, 500 mL of CTAB 100 mM were stirred at 30 °C. 500 µL of $AgNO_3$ 100 mM were added, followed by 10 mL of $HAuCl_4$ 25 mM, 10 mL of HCl 1 M, 4 mL of AA 100 mM and 4.0 mL of seeds. After 4 h at 30 °C, the bipyramids were centrifuged twice to remove excess f reactants. To increase the shape yield, the bipyramids were purified by depletion during one night at 30 °C in BDAC (350 mM),[74] after which the supernatant was discarded, and the precipitate redispersed in water and washed twice with 10 mM CTAC. The AuBPs were finally redispersed in 2 mL of 10 mM CTAC.

*Ligand Exchange Reaction – Phase Transfer*: To ensure optimal reaction conditions, i.e., to introduce as little water as possible into the reaction medium, hydrophilic AuBPs were concentrated by centrifugation at 9000 rpm for 5 min. The supernatant was discarded, and the pellet was dispersed drop by drop in a mixture of ligands (L and DDT) in THF in an ultrasonic bath. The reaction was left under these conditions for 5 min. In a typical process, the molar ratio of $Au^0$ to L to DDT was 1:2:1. The L concentration was 1 mM. To purify AuBPs, obtained NPs were centrifuged at 9000 rpm for 10 min. The supernatant was carefully separated, and the pellet was dispersed in a fresh portion of THF.

*Preparation of Helical Nanocomposites with NPs*: 50 µL of OIM THF solution (4 mg $mL^{-1}$) was mixed with 50 µL of chiral dopant (0.4 mg $mL^{-1}$) and with an appropriate amount (2–25% relative to the weight of the matrix) of NBPs (0.1 mM). Subsequently, the mixture was dropcasted onto a standard (10 mm x 10 mm) cover glass at 75 °C. The composite film was then heated to 150 °C and cooled to room temperature at 9 °C $min^{-1}$ using a Linkam heating stage. For the heating/cooling experiments, samples were cycled between rt and 150 °C with the same heating/cooling rates as above.

*Structural Characterization*: The shape and size of NPs, as well as their self-assembly into helical structures, were examined by TEM (JEOL-1400, JEOL Co. Japan), equipped with a high-resolution digital camera CCD MORADA G2 (EMSIS GmbH, Germany) available at the Nencki Institute of Experimental Biology of the Polish Academy of Sciences, Laboratory of Electron Microscopy.

*Optical Characterization*: Spectroscopic study of the materials in the colloid in the UV–vis range was performed using a GENESYS 50 UV–vis spectrometer, available at the University of Warsaw. The spectra of the functionalized nanoparticles were performed in THF solutions, using quartz cuvettes with a 2 mm optical path. Circular Dichroism measurements were performed using a Chirascan Circular Dichroism Spectrometer by Applied PhotoPhysics, available at the University of Warsaw.

*Mueller Matrix Polarimetry (MMP)*: MMP and spatial mapping of CD (iCD) were performed at the B23 beamline of the Diamond Light Source using the methodology developed by Siligardi et al.[56,75] The CD spectra were ac-quired in the 350–650 nm range, and the maps collected at 400 or 530 nm were obtained by rastering samples across a 50 µm light beam using a motorized XY-translation stage.

## Supporting Information

Supporting Information is available from the Wiley Online Library or from the author.

## Acknowledgements

M.W. and W.L. acknowledge support from the PRELUDIUM project 2021/41/N/ST5/04412 of the National Science Centre, Poland. M.P. and W.L. acknowledge support from the Preludium Bis project 2020/39/O/ST5/03445 of the National Science Centre, Poland. C.H. acknowledge the ANR CODENAME (ANR-23-CE09-0032), METATRAP (ANR-22-CE09-0011) and CNRS for funding. L.R. acknowledges support by the Karlsruhe School of Optics & Photonics (KSOP). L.R. and C.R. acknowledge financial support by the Deutsche Forschungsgemeinschaft (DFG, German Research Foundation) – Project-ID 258734477 – SFB 1173. The authors are grateful to the company JCMwave for their free provision of the FEM Maxwell solver JCMsuite.

## Conflict of Interest

The authors declare no conflict of interest.

## Data Availability Statement

The data that support the findings of this study are available from the corresponding author upon reasonable request.

## Keywords

chiral plasmonics, dynamically switchable structure and properties, gold bipyramids, helical nanofilaments, liquid crystals, reversible assembly, self-assembly

Received: January 10, 2025
Revised: April 28, 2025
Published online:

[1] S. Hou, H. Zhang, J. Yan, Y. Ji, T. Wen, W. Liu, Z. Hu, X. Wu, *Phys. Chem. Chem. Phys.* **2015**, *17*, 8187.
[2] X. Lu, X. Wang, Y. Liu, T. Ding, *Proc. Natl. Acad. Sci. USA* **2023**, *120*, 2216627120.
[3] L. Liu, Y. Yang, S. C. J. Meskers, Q. Wang, L. Zhang, C. Yang, J. Zhang, L. Zhu, Y. Zhang, Z. Wei, *Adv. Mater.* **2023**, *35*, 2304627.
[4] N.-N. Zhang, M. Mychinko, S.-Y. Gao, L. Yu, Z.-L. Shen, L. Wang, F. Peng, Z. Wei, Z. Wang, W. Zhang, S. Zhu, Y. Yang, T. Sun, L. M. Liz-Marzán, S. Bals, K. Liu, *Nano Lett.* **2024**, *24*, 13027.
[5] J. Gao, W. Wu, V. Lemaire, A. Carvalho, S. Nlate, T. Buffeteau, R. Oda, Y. Battie, M. Pauly, E. Pouget, *ACS Nano* **2020**, *14*, 4111.
[6] Y. He, H. Li, A. M. Steiner, A. Fery, Y. Zhang, C. Ye, *Adv. Mater.* **2023**, *35*, 2303595.
[7] G. Cheng, D. Xu, Z. Lu, K. Liu, *ACS Nano* **2019**, *13*, 1479.
[8] L. A. Warning, A. R. Miandashti, L. A. McCarthy, Q. Zhang, C. F. Landes, S. Link, *ACS Nano* **2021**, *15*, 15538.
[9] S. Link, G. V. Hartland, *J. Phys. Chem. C* **2021**, *125*, 10175.
[10] B. Ni, G. González-Rubio, K. Van Gordon, S. Bals, N. A. Kotov, L. M. Liz-Marzán, *Adv. Mater.* **2024**, *36*, 2412473.
[11] J. Kumar, K. G. Thomas, L. M. Liz-Marzán, *Chem. Commun.* **2016**, *52*, 12555.
[12] S. Both, M. Schäferling, F. Sterl, E. A. Muljarov, H. Giessen, T. Weiss, *ACS Nano* **2022**, *16*, 2822.
[13] P. T. Probst, Y. Dong, Z. Zhou, O. Aftenieva, A. Fery, *Adv. Opt. Mater.* **2024**, *12*, 2301834.
[14] L. Yang, C. Kwan, L. Zhang, X. Li, Y. Han, K. C. Leung, Y. Yang, Z. Huang, *Adv Funct Materials* **2019**, *29*, 1807307.
[15] B. Ni, M. Mychinko, S. Gómez-Graña, J. Morales-Vidal, M. Obelleiro-Liz, W. Heyvaert, D. Vila-Liarte, X. Zhuo, W. Albrecht, G. Zheng, G. González-Rubio, J. M. Taboada, F. Obelleiro, N. López, J. Pérez-Juste, I. Pastoriza-Santos, H. Cölfen, S. Bals, L. M. Liz-Marzán, *Adv. Mater.* **2023**, *35*, 2208299.
[16] Y. Wang, X. Zhang, D. Xie, C. Chen, Z. Huang, Z. A. Li, *Adv Funct Materials* **2025**, *35*, 2419610.
[17] Y. Yao, T. J. Ugras, T. Meyer, M. Dykes, D. Wang, A. Arbe, S. Bals, B. Kahr, R. D. Robinson, *ACS Nano* **2022**, *16*, 20457.
[18] Y. Negrín-Montecelo, A. Movsesyan, J. Gao, S. Burger, Z. M. Wang, S. Nlate, E. Pouget, R. Oda, M. Comesaña-Hermo, A. O. Govorov, M. A. Correa-Duarte, *J. Am. Chem. Soc.* **2022**, *144*, 1663.
[19] C. Chen, B. Ai, Y. Wang, Z. Xiao, G. Xiao, G. Zhang, *Adv Funct Materials* **2025**, *35*, 2409004.
[20] J. Lu, Y. Xue, K. Bernardino, N. N. Zhang, W. R. Gomes, N. S. Ramesar, S. Liu, Z. Hu, T. Sun, A. F. de Moura, N. A. Kotov, K. Liu, *Science* **2021**, *371*, 1368.
[21] Z. Li, Q. Fan, Z. Ye, C. Wu, Z. Wang, Y. Yin, *Science* **2023**, *380*, 1384.
[22] A. Querejeta-Fernández, B. Kopera, K. S. Prado, A. Klinkova, M. Methot, G. Chauve, J. Bouchard, A. S. Helmy, E. Kumacheva, *ACS Nano* **2015**, *9*, 10377.
[23] A. Querejeta-Fernández, G. Chauve, M. Methot, J. Bouchard, E. Kumacheva, *J. Am. Chem. Soc.* **2014**, *136*, 4788.
[24] J. Cheng, G. L. Saux, J. Gao, T. Buffeteau, Y. Battie, P. Barois, V. Ponsinet, M. H. Delville, O. Ersen, E. Pouget, R. Oda, *ACS Nano* **2017**, *11*, 3806.
[25] P. T. Probst, M. Mayer, V. Gupta, A. M. Steiner, Z. Zhou, G. K. Auernhammer, T. A. F. König, A. Fery, *Nat. Mater.* **2021**, *20*, 1024.
[26] H. Hu, S. Sekar, W. Wu, Y. Battie, V. Lemaire, O. Arteaga, L. V. Poulikakos, D. J. Norris, H. Giessen, G. Decher, M. Pauly, *ACS Nano* **2021**, *15*, 13653.
[27] H. E. Lee, H. Y. Ahn, J. Mun, Y. Y. Lee, M. Kim, N. H. Cho, K. Chang, W. S. Kim, J. Rho, K. T. Nam, *Nature* **2018**, *556*, 360.
[28] G. González-Rubio, J. Mosquera, V. Kumar, A. Pedrazo-Tardajos, P. Llombart, D. M. Solís, I. Lobato, E. G. Noya, A. Guerrero-Martínez, J. M. Taboada, F. Obelleiro, L. G. MacDowell, S. Bals, L. M. Liz-Marzán, *Science* **2020**, *368*, 1472.
[29] T. H. Chow, N. Li, X. Bai, X. Zhuo, L. Shao, J. Wang, *Acc. Chem. Res.* **2019**, *52*, 2136.
[30] Y. H. Lee, Y. Won, J. Mun, S. Lee, Y. Kim, B. Yeom, L. Dou, J. Rho, J. H. Oh, *Nat. Commun.* **2023**, *14*, 7298.
[31] D. Château, S. David, G. Berginc, C. Lopes, F. Chaput, F. Lerouge, A. Désert, C. Andraud, S. Parola, *ACS Appl. Nano Mater* **2022**, *5*, 3773.
[32] H. Zhang, J. Liu, *Opt. Lett.* **2016**, *41*, 1150.
[33] J.-H. Lee, Z. Cheglakov, J. Yi, T. M. Cronin, K. J. Gibson, B. Tian, Y. Weizmann, *J. Am. Chem. Soc.* **2017**, *139*, 8054.
[34] H. Kim, R. M. Kim, S. D. Namgung, N. H. Cho, J. B. Son, K. Bang, M. Choi, S. K. Kim, K. T. Nam, J. W. Lee, J. H. Oh, *Adv. Sci.* **2022**, *9*, 2104598.
[35] R. A. Nome, M. J. Guffey, N. F. Scherer, S. K. Gray, *J. Phys. Chem. A* **2009**, *113*, 4408.
[36] S. Nafisah, M. Morsin, R. Sanudin, N. L. Razali, Z. M. Zain, M. Djamal, *IEEE Sensors J* **2022**, *22*, 18479.
[37] S. Xu, W. Ouyang, P. Xie, Y. Lin, B. Qiu, Z. Lin, G. Chen, L. Guo, *Anal. Chem.* **2017**, *89*, 1617.
[38] J. Feng, L. Chen, Y. Xia, J. Xing, Z. Li, Q. Qian, Y. Wang, A. Wu, L. Zeng, Y. Zhou, *ACS Biomater. Sci. Eng.* **2017**, *3*, 608.

[39] I. Song, X. Shang, J. Ahn, J. H. Lee, W. Choi, H. Ohtsu, J. C. Kim, S. K. Kwak, J. H. Oh, *Chem. Mater.* **2022**, *34*, 8675.
[40] H. K. Yip, X. Zhu, X. Zhuo, R. Jiang, Z. Yang, J. Wang, *Adv. Opt. Mater.* **2017**, *5*, 1700740.
[41] J. R. G. Navarro, F. Lerouge, G. Micouin, C. Cepraga, A. Favier, M. T. Charreyre, N. P. Blanchard, J. Lermé, F. Chaput, M. Focsan, K. Kamada, P. L. Baldeck, S. Parola, *Nanoscale* **2014**, *6*, 5138.
[42] A. Carone, P. Mariani, A. Désert, S. Parola, *Adv. Opt. Mater.* **2023**, *11*, 2300119.
[43] Z. Mai, Y. Yuan, J. B. Tai, B. Senyuk, B. Liu, H. Li, Y. Wang, G. Zhou, I. I. Smalyukh, *Adv. Sci.* **2021**, *8*, 2102854.
[44] H. Ayeb, J. Grand, H. Sellame, S. Truong, J. Aubard, N. Felidj, A. Mlayah, E. Lacaze, *J. Mater. Chem.* **2012**, *22*, 7856.
[45] S.-P. Do, A. Missaoui, A. Coati, D. Coursault, H. Jeridi, A. Resta, N. Goubet, M. M. Wojcik, A. Choux, S. Royer, E. Briand, B. Donnio, J. L. Gallani, B. Pansu, E. Lhuillier, Y. Garreau, D. Babonneau, M. Goldmann, D. Constantin, B. Gallas, B. Croset, E. Lacaze, *Nano Lett.* **2020**, *20*, 1598.
[46] R. Pardehkhorram, S. Bonaccorsi, H. Zhu, V. R. Gonçales, Y. Wu, J. Liu, N. A. Lee, R. D. Tilley, J. J. Gooding, *Chem. Commun.* **2019**, *55*, 7707.
[47] X. Li, J. Lyu, C. Goldmann, M. Kociak, D. Constantin, C. Hamon, *J. Phys. Chem. Lett.* **2019**, *10*, 7093.
[48] J. Lyu, W. Chaâbani, E. Modin, A. Chuvilin, T. Bizien, F. Smallenburg, M. Impéror-Clerc, D. Constantin, C. Hamon, *Adv. Mater.* **2022**, *34*, 2200883.
[49] P. Chen, G. Wang, C. Hao, W. Ma, L. Xu, H. Kuang, C. Xu, M. Sun, *Chem. Sci.* **2022**, *13*, 10281.
[50] W. Liu, D. Liu, Z. Zhu, B. Han, Y. Gao, Z. Tang, *Nanoscale* **2014**, *6*, 4498.
[51] D. Grzelak, M. Tupikowska, D. Vila-Liarte, D. Beutel, M. Bagiński, S. Parzyszek, M. Góra, C. Rockstuhl, L. M. Liz-Marzán, W. Lewandowski, *Adv Funct Materials* **2022**, *32*, 2111280.
[52] Y. He, X. Meng, Z. Shen, B. Jin, X. Chen, B. Ai, K. Liu, C. Ye, *Small* **2025**, *21*, 2407635.
[53] M. Bagiński, M. Tupikowska, G. González-Rubio, M. Wójcik, W. Lewandowski, *Adv. Mater.* **2020**, *32*, 1904581.
[54] D. Chateau, A. Liotta, F. Vadcard, J. R. G. Navarro, F. Chaput, J. Lermé, F. Lerouge, S. Parola, *Nanoscale* **2015**, *7*, 1934.
[55] J. Lyu, F. Rondepierre, C. Jonin, P.-F. Brevet, C. Hamon, D. Constantin, *J. Phys. Chem. C* **2022**, *126*, 9831.
[56] P. Szustakiewicz, F. Powała, D. Szepke, W. Lewandowski, P. W. Majewski, *Adv. Mater.* **2024**, *36*, 2310197.
[57] N. Kowalska, F. Bandalewicz, J. Kowalski, S. Gómez-Graña, M. Bagiński, I. Pastoriza-Santos, M. Grzelczak, J. Matraszek, J. Pérez-Juste, W. Lewandowski, *ACS Appl. Mater. Interfaces* **2022**, *14*, 50013.
[58] S. Parzyszek, J. Tessarolo, A. Pedrazo-Tardajos, A. M. Ortuño, M. Bagiński, S. Bals, G. H. Clever, W. Lewandowski, *ACS Nano* **2022**, *16*, 18472.
[59] W. Park, D. K. Yoon, *Crystals* **2020**, *10*, 675.
[60] P. J. Stephens, N. Harada, *Chirality* **2010**, *22*, 229.
[61] R. M. A. Azzam, *J. Opt. Soc. Am.* **1978**, *68*, 1756.
[62] M. Magnozzi, M. Ferrera, L. Mattera, M. Canepa, F. Bisio, *Nanoscale* **2019**, *11*, 1140.
[63] JCMwave GmbH, JCMsuite version 6.0.10, https://jcmwave.com/jcmsuite.
[64] M. I. Mishchenko, L. D. Travis, D. W. Mackowski, *J. Quant. Spectrosc. Radiat. Transfer* **1996**, *55*, 535.
[65] N. Asadova, K. Achouri, K. Arjas, B. Auguié, R. Aydin, A. Baron, D. Beutel, B. Bodermann, K. Boussaoud, S. Burger, M. Choi, K. M. Czajkowski, A. B. Evlyukhin, A. Fazel-Najafabadi, I. Fernandez-Corbaton, P. Garg, D. Globosits, U. Hohenester, H. Kim, S. Kim, P. Lalanne, E. C. Le Ru, J. Meyer, J. Mun, L. Pattelli, L. Pflug, C. Rockstuhl, J. Rho, S. Rotter, B. Stout, et al., *J. Quant. Spectrosc. Radiat. Transfer* **2025**, *333*, 109310.
[66] D. Beutel, I. Fernandez-Corbaton, C. Rockstuhl, *Comput. Phys. Commun.* **2024**, *297*, 109076.
[67] R. Nag, N. Rouvière, J. G. Trazo, J. Marcone, N. Kutalia, C. Goldmann, M. Impéror-Clerc, D. Alloyeau, D. Constantin, C. Hamon, *Nano Lett.* **2024**, *24*, 16368.
[68] M. Künzle, T. Eckert, T. Beck, *J. Am. Chem. Soc.* **2016**, *138*, 12731.
[69] R. J. Macfarlane, B. Lee, M. R. Jones, N. Harris, G. C. Schatz, C. A. Mirkin, *Science* **2011**, *334*, 204.
[70] F. Lu, K. G. Yager, Y. Zhang, H. Xin, O. Gang, *Nat. Commun.* **2015**, *6*, 6912.
[71] K. Aliyah, J. Lyu, C. Goldmann, T. Bizien, C. Hamon, D. Alloyeau, D. Constantin, *J. Phys. Chem. Lett.* **2020**, *11*, 2830.
[72] A. Sánchez-Iglesias, N. Winckelmans, T. Altantzis, S. Bals, M. Grzelczak, L. M. Liz-Marzán, *J. Am. Chem. Soc.* **2017**, *139*, 107.
[73] C. Goldmann, M. De Frutos, E. H. Hill, D. Constantin, C. Hamon, *Chem. Mater.* **2021**, *33*, 2948.
[74] J.-H. Lee, K. J. Gibson, G. Chen, Y. Weizmann, *Nat. Commun.* **2015**, *6*, 7571.
[75] R. Hussain, T. Jávorfi, G. Siligardi, *Front. Chem.* **2021**, *9*, 616928.